Journal of Sustainable Metallurgy (2021) 7:391–405
https://doi.org/10.1007/s40831-021-00374-y

THEMATIC SECTION: MOLTEN 2021: SLAGS, FLUXES, AND SALTS FOR ENVIRONMENT, RECYCLING, AND SUSTAINABILITY

Phase Transition of Ca- and Mg-Bearing Minerals of Steel Slag in Acidic Solution for CO_2 Sequestration

Xiaohui Mei[1,2] · Qing Zhao[1,2] · Junye Zhou[2] · Xinyu Lang[2] · Yi Min[1,2] · Henrik Saxén[3] · Ron Zevenhoven[3]

Received: 9 March 2021 / Accepted: 23 April 2021 / Published online: 14 May 2021

Abstract
Large amounts of steel slag (SS) and CO_2 are produced by the steel industry worldwide. Indirect aqueous carbonation of SS using Ca and Mg is a promising way for carbon capture, utilization, and storage (CCUS). However, some Ca and Mg enriched in refractory minerals affect the extraction efficiency. Therefore, understanding the phase transition of various Ca- and Mg-bearing minerals in strong or mild acidic solutions is of vital importance for SS-based CCUS. This work evaluated the leachability of common minerals of SS in an acidic solution based on thermodynamic analysis and leaching tests. The results showed that the order of leachability of the phases is as follows: CaO > ($Ca_3Al_2O_6$, γ-Ca_2SiO_4, $Ca_3MgSi_2O_8$, and $Ca_2MgSi_2O_7$) > ($Ca_{12}Al_{14}O_{33}$, $CaAl_2O_4$, and $Ca_2Fe_2O_5$). Under the experimental conditions employed in this study, an amorphous phase of silica gel and aluminum hydroxide formed in the dissolution process of $Ca_3MgSi_2O_8$, $Ca_3Al_2O_6$ and $Ca_{12}Al_{14}O_{33}$ phases, which covered the surface of the particles hindering further decomposition. Moreover, a Ca-depleted layer was observed after leaching of $Ca_2MgSi_2O_7$, $Ca_{12}Al_{14}O_{33}$, $CaAl_2O_4$, and $Ca_2Fe_2O_5$, and their phase transitions were studied and a mechanism was proposed in this work.

The contributing editor for this article was Sharif Jahanshahi.

✉ Qing Zhao
zhaoq@smm.neu.edu.cn

[1] Key Laboratory for Ecological Metallurgy of Multimetallic Mineral (Ministry of Education), Northeastern University, Shenyang 110819, China

[2] School of Metallurgy, Northeastern University, Mailbox 288, Wenhua Road, Heping District, Shenyang 110819, China

[3] Process and Systems Engineering Laboratory, Åbo Akademi University, 20500 Åbo/Turku, Finland

Graphical Abstract

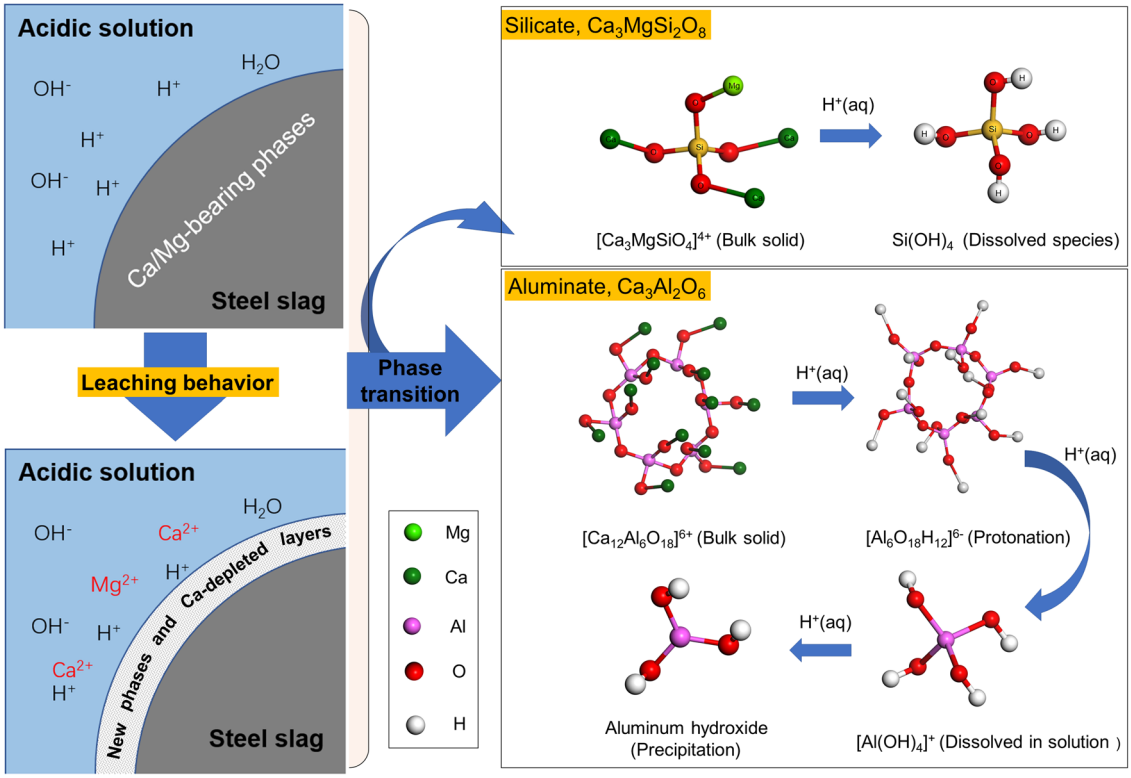

New phases or Ca-depleted layers formed on the surface of the Ca- and Mg-bearing mineral particles of steel slag after leaching in an acidic solution, and the phase transition behaviors and mechanisms are related to the crystal structure of the minerals.

Keywords Steel slag · Minerals · Indirect aqueous carbonation · CO_2 sequestration · Phase transition

Introduction

Steel slag (SS) and CO_2 are two major waste products of the iron and steelmaking process. The utilization of SS is still below 30% in some major steel-producing countries, such as China and India [1]. It is recognized that SS-based carbon capture, utilization, and storage (SS-based CCUS) process is a promising way for simultaneous mitigation of CO_2 emissions and re-exploitation of wastes [2]. At present, process of SS-based CCUS proposed can be divided into direct (gas-solid) routes and indirect (leaching or extraction before carbonation) routes [3]. The direct SS-based carbonation has been plagued by moderate kinetics [4]. It has been proposed that precipitated calcium carbonate (PCC) can be produced via indirect SS-based CCUS, by selective extraction of Ca^{2+} with an aqueous solution, such as acid (e.g., HCl, HNO_3, CH_3COOH, or HCOOH) and an ammonium salt (NH_4Cl, NH_4NO_3, or CH_3COONH_4) [5, 6]. However, the leaching of Ca from SS is often found to be incomplete and poor [7], which affects the efficiency of SS-based CCUS.

It is generally recognized that the low ion extraction yield and efficiency are attributed to the fact that Ca and Mg are distributed over various mineral or amorphous phases in SS [8]. Doucet [9] analyzed the mineralogical composition of SS before and after treatment with HNO_3 by X-ray diffractometer (XRD) and found that lime (CaO), larnite (Ca_2SiO_4), and calcite ($CaCO_3$) were the most reactive Ca-bearing phases, whereas brownmillerite ($Ca_2Fe_{1.4}Mg_{0.3}Si_{0.3}O_5$) was the most insoluble Ca phase. Likewise, the work of Raghavendra [10] suggested that the solubility characteristics of phases present in SS may be substantially different. Thus, it could be expected that the SS recovery yields may be improved by enriching Ca and Mg into water-soluble phases though controlling the crystallization process of the molten slag [11, 12]. The phase modification method has been applied in stainless steel slag for stabilization of Cr [13–15] due to the potential risk of toxic Cr^{6+} release [16, 17]. Recently, Zhao et al. [18] remediated stainless steel slag with MnO for the dual goals of Cr immobilization and Ca recovery. The results indicated that phase modification of SS

before an SS-based CCUS process is a promising pretreatment method that improves the carbonation efficiency. One of the targets of the work of the present paper is to clarify the leachability of various minerals ((Ca/Mg)-silicates, -aluminates, -ferrites, and oxides) and provide a reference for SS phase modification.

In addition, surface passivation behavior is another factor that affects the extraction of Ca, Mg, and Fe from SS, presumably based on the effect of particle size and the formation of a Si-rich layer [19, 20]. However, some results indicated that not all Ca-bearing silicate phases, such as pure dicalcium silicate (Ca_2SiO_4) and tricalcium silicate (Ca_3SiO_5), leave behind a Si-rich leached layer after dissolving as these mineral phases belong to the orthosilicate family [21]. Thus, there is still limited understanding of the mechanisms behind minerals leaching. The second goal of this work is to shed light on the phase transition behavior of each mineral during the leaching process.

This work systematically evaluated the leachability of common minerals ((Ca/Mg)-silicates, -aluminates, -ferrites, and oxides) in SS through thermodynamic calculations. Furthermore, several principal Ca-bearing phases were synthesized and a series of acid corrosion and leaching tests were carried out to study the leachability and leaching mechanisms.

Experimental

Raw Material Preparation and Characterization

A series of typical minerals encountered in argon oxygen decarburization (AOD) slag, electric arc furnace (EAF) slag, ladle furnace (LF) slag, and basic oxygen furnace (BOF) slag were synthesized by the twice-sintering method [22], including γ-dicalcium silicate (γ-Ca_2SiO_4, γ-C_2S), akermanite ($Ca_2MgSi_2O_7$, C_2MS_2), merwinite ($Ca_3MgSi_2O_8$, C_3MS_2), calcium aluminate ($CaAl_2O_4$, CA), mayenite ($Ca_{12}Al_{14}O_{33}$, $C_{12}A_7$), tricalcium aluminate ($Ca_3Al_2O_6$, C_3A), and dicalcium ferrite ($Ca_2Fe_2O_5$, C_2F) phases. The specific types of minerals, sintering parameters, and melting point [23, 24] are presented in Table 1 for the seven synthetic mixtures. Analytical grade calcium oxide (CaO), magnesium oxide (MgO), silica (SiO_2), aluminum oxide (Al_2O_3), and hematite (Fe_2O_3) were used for synthesis. The chemicals were stoichiometrically blended in a ball mill under ambient conditions for each mineral. In all milling runs, the agate ball to powder weight ratio was 10:1. The rotational speed was set at 200 rpm during the milling process for 120 min. After that, the resultant mixture (15 g) was briquetted into a round pie (4 cm in diameter, ~ 0.8 cm in thickness) under 30 MPa to achieve good contact between the particles. The pressed tablets were fired in a furnace at the air atmosphere twice to obtain a pure mineral phase, with grinding and briquetting between firings. The twice-sintered samples were cooled in the furnace for use. In addition, the CaO phase was chemically pure without firing.

The purity of synthetic minerals was confirmed by powered X-ray diffraction (XRD) using a Philips X'Pert X-ray diffractometer, equipped with copper *kα* radiation. The XRD pattern was recorded in the 2-theta range 10–70°, counting $4°\cdot min^{-1}$.

Thermodynamic Analysis

The decomposition thermodynamics in an HCl solution of the minerals was computationally analyzed by FactSage (version 8.0) using a reaction model. The computational minerals include silicates ($CaSiO_3$, γ-Ca_2SiO_4, α-Ca_2SiO_4, Ca_3SiO_5, $Ca_3Si_2O_7$, $Ca_2MgSi_2O_7$, $Ca_3MgSi_2O_8$, and $CaMgSi_2O_6$), aluminates ($CaAl_2O_4$, $Ca_3Al_2O_6$), ferrites ($CaFe_2O_4$, $Ca_2Fe_2O_5$), and RO phases (CaO, FeO, and Fe_2O_3). The phases of calcium aluminate ($C_{12}A_{14}O_{33}$, $C_{12}A_7$) and β-dicalcium silicate (β-Ca_2SiO_4, β-C_2S) were excluded from the decomposition thermodynamic calculation due to a lack of relevant thermodynamic data, which is likely because of its metastable behavior [25]. The thermodynamic data of the minerals and solution were based on the FToxid, FThelg, and FactPS databases. The thermodynamic data of available phases were all at a temperature of 298–373 K and 1 atm.

Table 1 Phase types, sintering parameters, and melting point of synthesized mineral mixtures

Phase type	Synthesized minerals	Sintering temperature (K)	Sintering time (h)	Melting point (K)
Silicate	γ-Dicalcium silicate (γ-Ca_2SiO_4, γ-C_2S)	1673	24	2403
	Akermanite ($Ca_2MgSi_2O_7$, C_2MS_2)	1673	24	1731
	Merwinite ($Ca_3MgSi_2O_8$, C_3MS_2)	1673	48	1871
Aluminate	Calcium aluminate ($CaAl_2O_4$, CA)	1773	24	1878
	Mayenite ($Ca_{12}Al_{14}O_{33}$, $C_{12}A_7$)	1673	24	1686
	Tricalcium aluminate ($Ca_3Al_2O_6$, C_3A)	1623	24	1808
Ferrite	Dicalcium ferrite ($Ca_2Fe_2O_5$, C_2F)	1673	24	1711

Leaching Testing

A series of leaching experiments were undertaken to investigate the leachability of the studied minerals in acidic solutions. For this purpose, 2 g of the mineral combined with 250 mL of 0.1 mol·L^{-1} HCl was added to the reaction vessel for each experiment. To avoid particle size influence on the dissolution kinetics, a size fraction of 50–74 μm was used for all samples. A magnetic stirrer was applied at a constant stirring speed of 500 rpm during the leaching process, except for the studies of the C_2F phase, where mechanical stirring was used. The leaching experiments were carried out at room temperature for 2 h. After this, the slurry was filtered through 0.45 μm membrane filters under reduced pressure (about −0.1 MPa) in a filtration vessel to yield a leachate and then moved into a 500 mL volumetric flask. The concentration of dissolved Ca in the leachate was determined by plasma-optical emission spectrometry (ICP-OES) and chemical analysis. The leachability of minerals was assessed based on the Ca extracted to a 0.1 mol·L^{-1} HCl solution, and the leaching yield of Ca was determined as

$$R = \frac{C_{Ca} \times M_{Ca} \times V}{m \times w_{Ca}} \times 100\%$$

where C_{Ca} is the concentration of Ca^{2+} in the leachate (mol·L^{-1}), M_{Ca} is the molar mass of calcium (g·mol^{-1}), V is the volume of leachate (L), m represents the sample mass of minerals powder (g), and w_{Ca} is the stoichiometrical mass fraction of Ca in the minerals.

To study the dissolution mechanism of minerals, a series of surface corrosion experiments of minerals were carried out in HCl solution (0.1 mol·L^{-1}, 250 mL) at room temperature. Six sample minerals briquettes (γ-C_2S powder) were grinded and polished to produce smooth and flat surfaces. No water or alcohol was used during the grinding and polishing process since silicates and aluminates are easily hydrated [26]. The mineral phases after grinding and polishing were placed in six glass beakers containing HCl solution (0.1 mol·L^{-1}, 250 mL), respectively. After 48 h of corrosion reaction at room temperature, the sample was removed and the corroded surface was carefully rinsed with deionized water to wash off the residual ions, such as Cl^-, Ca^{2+}, and Mg^{2+}. After that, all the corroded phases were dried at 90 ℃ for 10 h. Before and after the corrosion test, all investigated samples were analyzed by scanning electron microscope (SEM), equipped with energy-dispersive X-ray spectroscopy (EDS). Furthermore, the surface roughness after acid corrosion was measured with an Olympus 3D measuring laser microscope (3DMLM).

Results and Discussion

Characterization of Synthetic Mineral Phase

XRD patterns of the synthetic mineral phases are shown in Fig. 1. The main peaks corresponding to the synthetic phases are marked with a star in the diffractograms. Most of the minerals synthesized by twice-sintering are relatively pure. In the C_3A phase, traces of $C_{12}A_7$ were detected.

The lattice constants of the seven synthesized minerals were calculated by the WPPD (whole powder pattern fitting) method [27], as shown in Table 2.

Theoretical Analysis

Figure 2 presents the enthalpy change (ΔH) of decomposition as a function of temperature in the range of 298–373 K for a series of pure minerals in HCl solution based on FactSage 8.0. It is seen that the decomposition reactions of silicate, aluminate, ferrite, and RO phases in the acidic solution are all exothermic ($\Delta H < 0$), which implies that increasing the temperature (298–373 K) promotes the ion extraction from the minerals. The findings are consistent with the experimental results of Doucet [9]. Furthermore, temperature is seen to have a slight effect on the ΔH of the dissolution reactions in the solution.

The Gibbs free energy (ΔG) of the extraction reactions were calculated using FactSage 8.0 software. As shown in Fig. 3, according to thermodynamics, all the aluminate, ferrite, and silicate phases can release Ca^{2+} and Mg^{2+} ions in the acidic solution at room temperature. The Fe^{2+} can be thermodynamically eluted from FeO. The decomposition reaction of Fe_2O_3 is thermodynamically limited at 298–373 K, which indicates that Fe^{3+} cannot, in theory, be eluted from hematite (Fe_2O_3) under the studied conditions. This may be a good result for iron recycling, since the high-valent iron (Fe^{3+}) can be enriched in leaching residue.

A more negative value of ΔG means better conditions for a spontaneous reaction. Therefore, from the perspective of thermodynamics, the leachability of minerals was evaluated based on the ΔG of the reaction of a unit mole of minerals with acidic solution. A diagram of the reaction advantage region of the studied minerals in the here used acidic solution at 298 K is shown in Fig. 4. The area where $\Delta G < -$ 400 kJ (equilibrium constant K is about 10^70) was taken to correspond to a high-reactivity zone, the area with $-$ 400 kJ $< \Delta G <$ $-$ 190 kJ (10^33 $< K <$ 10^70) to a reactivity zone, and the area with $\Delta G >$ $-$ 190 kJ (equilibrium constant K is about 10^33) to an inert zone. The

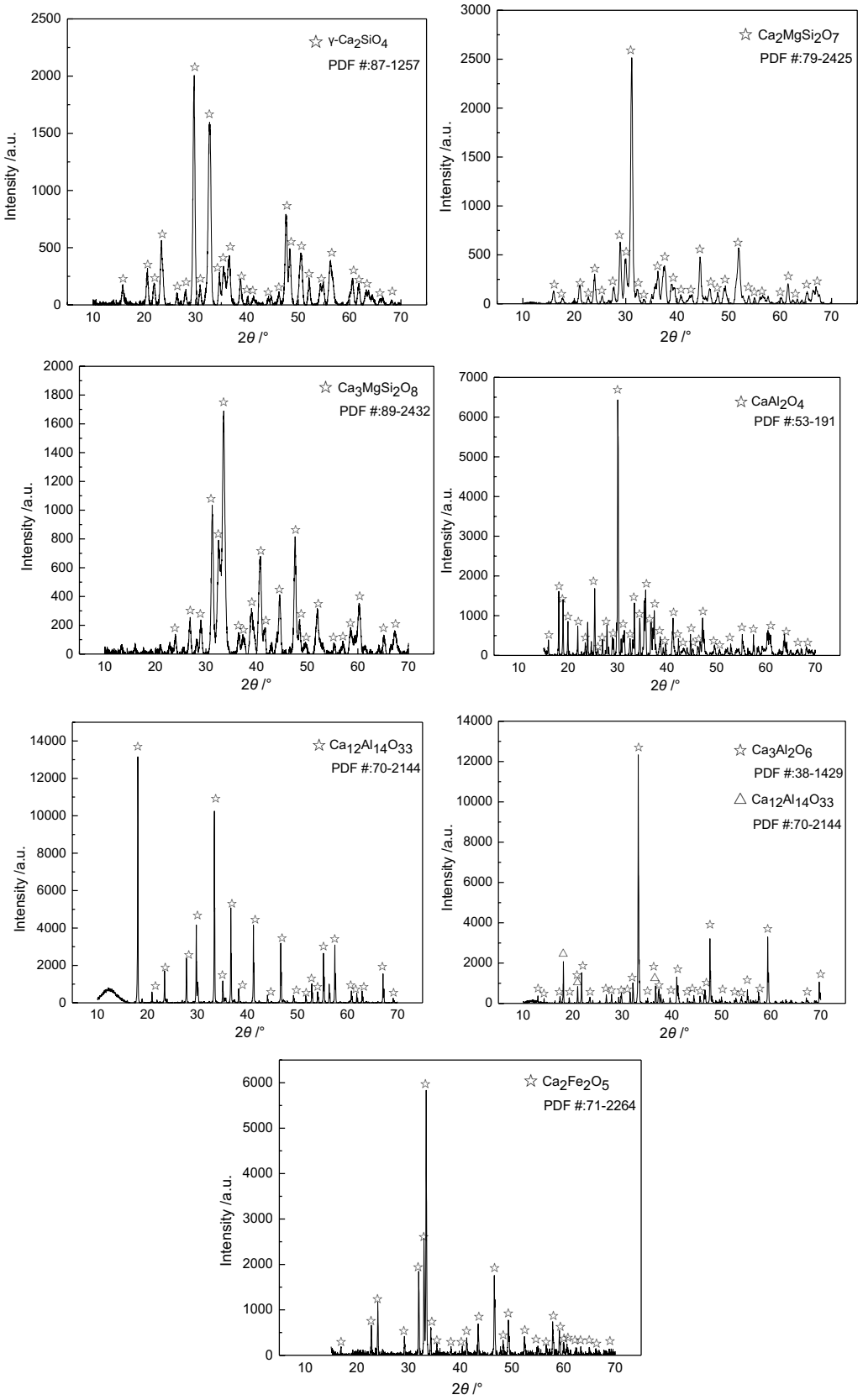

Fig. 1 XRD patterns of the seven synthetic mineral mixtures

Table 2 Crystallographic data for the minerals in the synthetic mixtures

Minerals	System	Space group	a (Å)	b (Å)	c (Å)	α (°)	β (°)	γ (°)
γ-C_2S	Orthorhombic	Pbnm	5.124	11.344	6.809	90	90	90
C_2MS_2	Tetragonal	P-421 m	7.907	7.907	5.053	90	90	90
C_3MS_2	Monoclinic	P21/c	9.468	5.351	13.394	90	92	90
CA	Monoclinic	P21/c	8.783	8.216	17.653	90	119	90
$C_{12}A_7$	Cubic	I-43d	11.981	11.981	11.981	90	90	90
C_3A	Cubic	Pa3	15.409	15.409	15.409	90	90	90
C_2F	Orthorhombic	Pnma	5.395	14.675	5.570	90	90	90

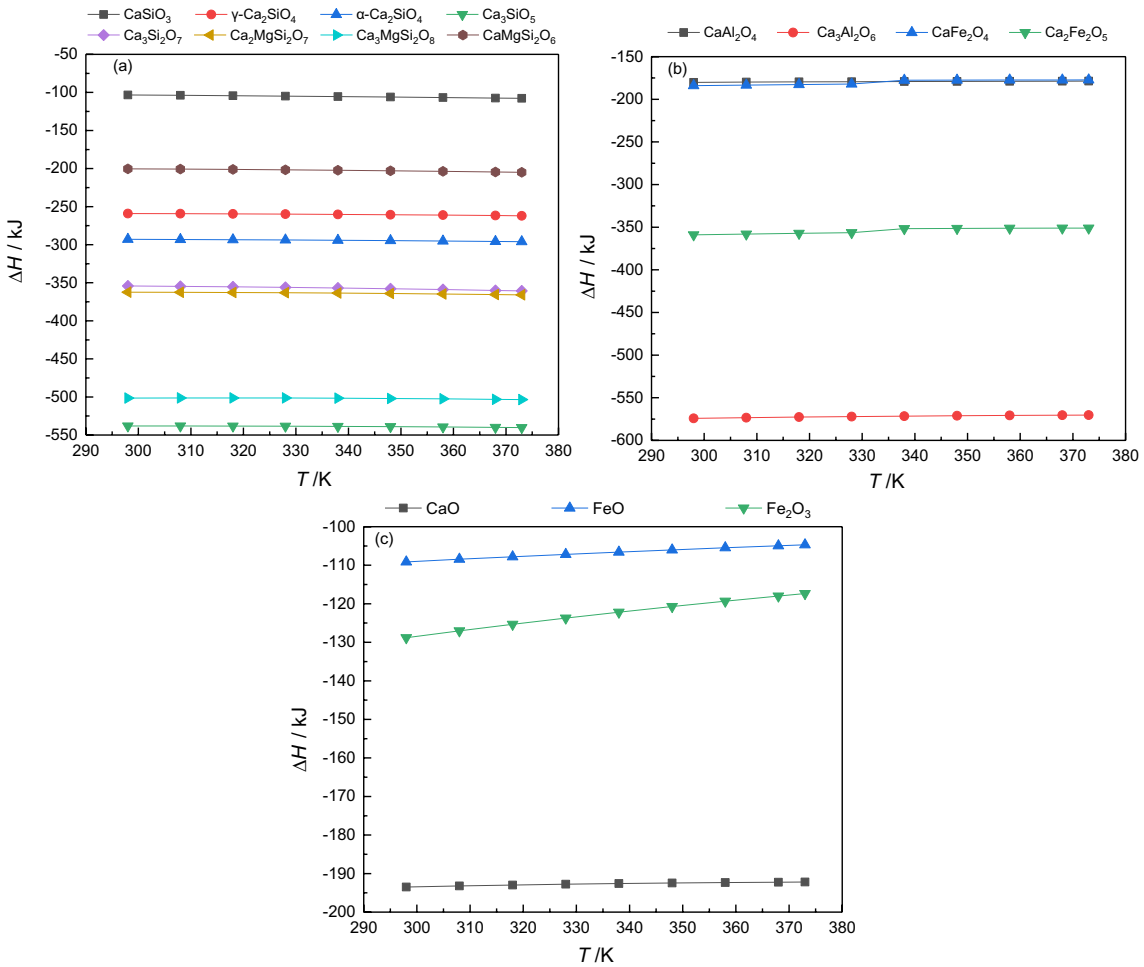

Fig. 2 Enthalpy change (ΔH) of reactions between the studied **a** silicate, **b** ferrite, and aluminate and **c** RO mineral phases and HCl acidic solution in the temperature range from 298 to 373 K, computationally

phases existing in the corresponding areas were correspondingly called high-reactive phase, reactive phase, and inert phase. As shown in Fig. 4 C_3A, C_3S, and C_3MS_2 are highly reactive phases, C_3S_2, C_2F, C_2MS_2, α-C_2S, γ-C_2S, and CaO are reactive phases, while the remaining six minerals are inert phases for the decomposition reaction.

Leaching Behavior

Understanding the dissolution character of minerals is essential for resource recovery and utilization. Herein, a batch of leaching tests were processed at room temperature, aimed to assess and compare the leachability of primary Ca-bearing

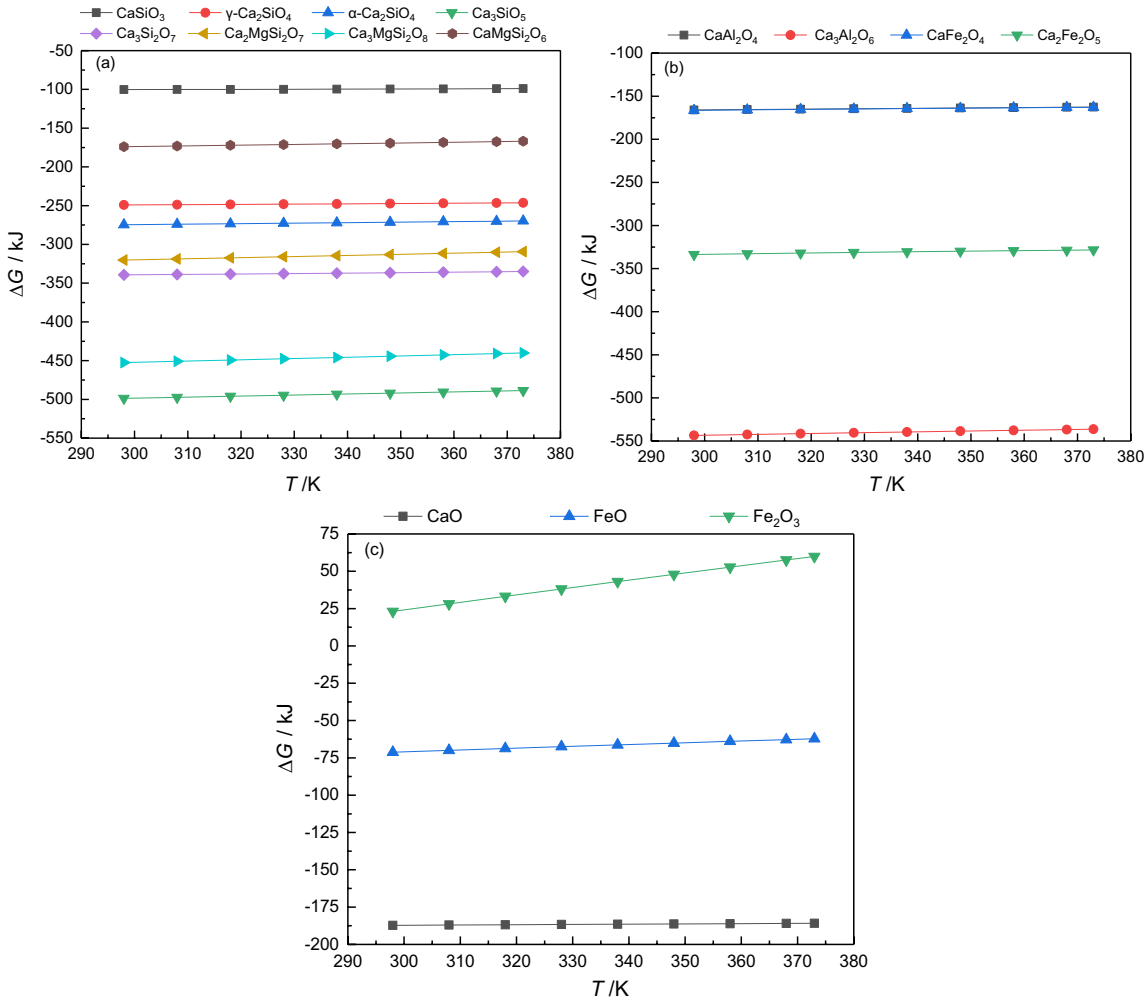

Fig. 3 Gibbs free energy change (ΔG) of reactions between the studied **a** silicate, **b** ferrite, and aluminate, and **c** RO phases and HCl acidic solution in the temperature range from 298 to 373 K, computationally

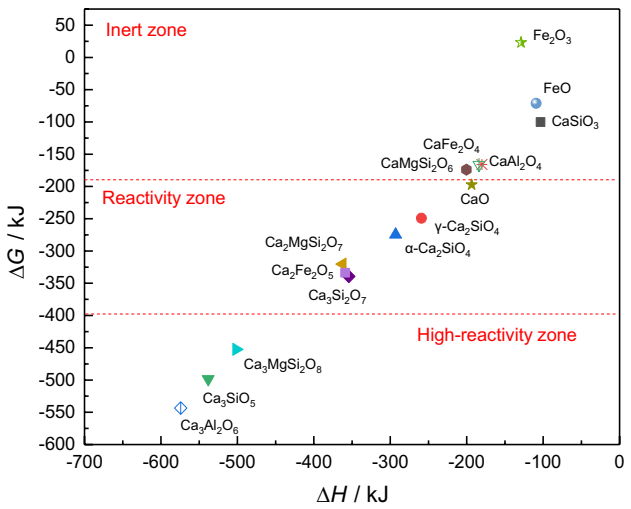

Fig. 4 Reaction advantage region diagram of the studied mineral phases in acidic solution at 298 K

phases in SS (silicate, aluminate, ferrite, and CaO phases). Figure 5 shows that the different types of mineral elicit a distinct Ca extraction yield. CaO shows a relatively high solubility (Ca^{2+} leaching yield > 80%), followed by the silicates (leaching yield > 45%), and most of the aluminates and ferrite, which were classified as inert phases (leaching yield < 30%). The experimental results are roughly consistent with findings of the thermodynamic calculations.

Similar experimental results were obtained in ammonium salt solutions. The CaO phase is the more reactive Ca-bearing phases [22], which indicates that SS containing a high proportion of free CaO may be especially desirable for Ca extraction and utilization [28, 29]. Indeed, Teir and Eloneva [5, 6] reported that around 30% of calcium from BOF slag can be leached out with water. However, SS generally contains a minor amount of free CaO, while silicates and aluminates are the primary Ca/Mg-bearing phases [30]. In this work, the aluminates ($C_{12}A_7$ and CA) were categorized

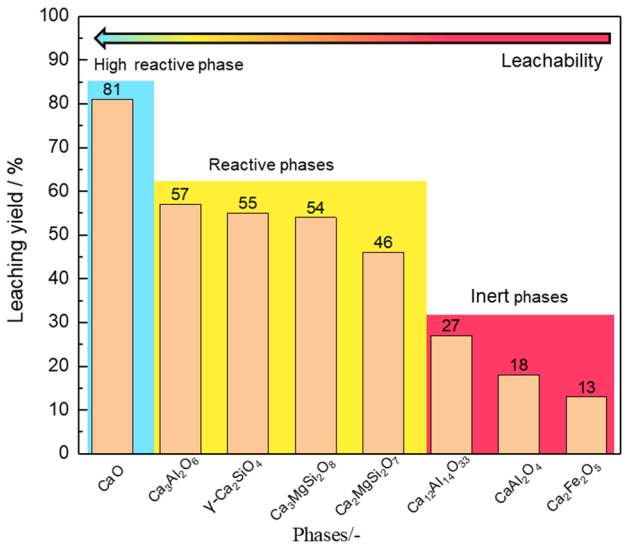

Fig. 5 Leaching yield of calcium from various minerals in 0.1 mol·L^{-1} HCl solution at room temperature

as inert phases, so another leaching process may be chosen for Al-rich SS followed by carbonation. The leaching yield of the C_2F phase is 13%, which means that a considerable amount of Fe will be presented in the non-dissolved leached slag residues. This demonstrates that it is promising to meet the dual goals of carbon sequestration and iron recovery in a CCUS process using SS.

The different Ca-containing phases gave different Ca dissolution under the present experimental conditions. Intriguingly, there is a discrepancy between the theoretical and experimental leachability of some minerals, especially for the C_2F phase. It is expected that the difference is related to the dissolution behavior and crystal structure of the minerals, or the quality or applicability of the thermodynamic data for these silicates for the current calculations.

Leaching Mechanism

It is necessary to establish the relationship between the crystal structure and the dissolution mechanism, which can help understand and predict the leachability of the phases. CaO usually has a high leachability due to its simple CaO bonding mode [31]. This section aims to provide insight into the leaching mechanism of the minerals (silicates, aluminates, and ferrite) based on the crystal structure.

Silicates

SEM–EDS and 3DMLM were employed to examine the morphology features of minerals before and after corrosion. As shown in Fig. 6, it can be observed that the surface

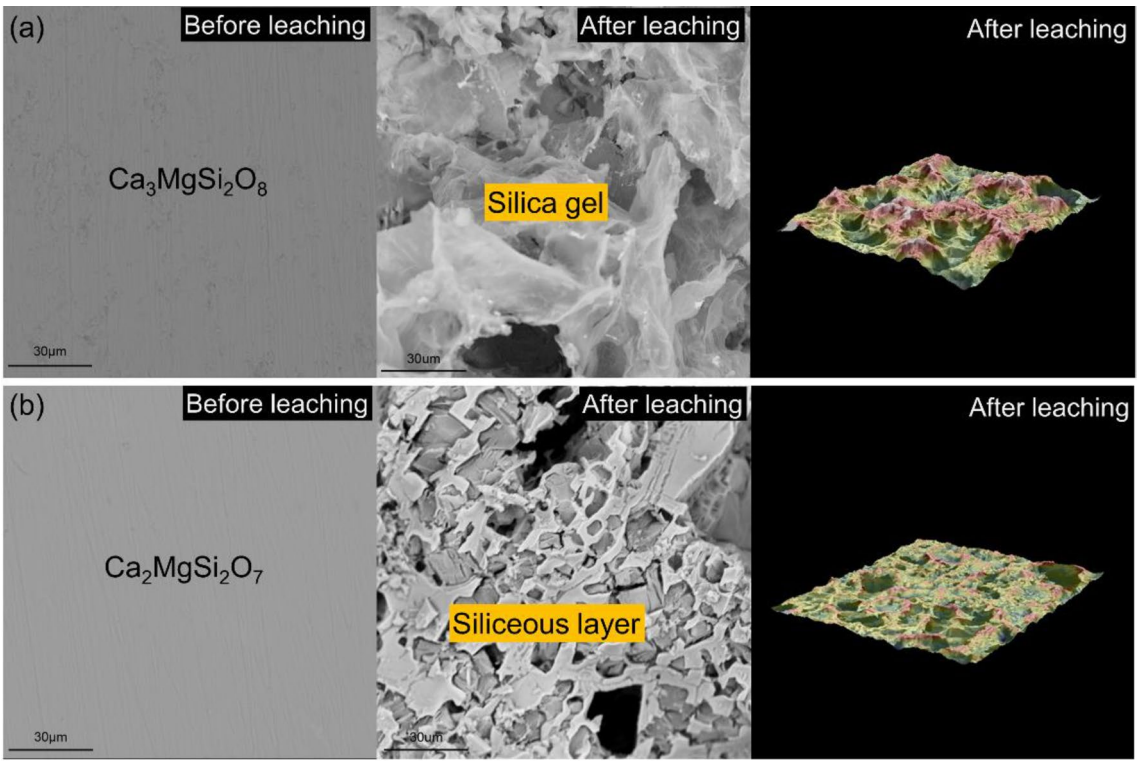

Fig. 6 SEM images and 3DMLM image of **a** C_3MS_2 and **b** C_2MS_2 briquettes before and after 0.1 mol·L^{-1} HCl leaching for 48 h and 90 °C drying for 10 h

before leaching was smooth and turned rugged after 48 h of leaching. Etch pits of different depths appeared on the surfaces of the two silicates during leaching. A thin and bright layer was observed on the C_3MS_2 phase surface after leaching (Fig. 6a), and a similar was observed in the BOF slag after treatment with ammonium salt [20]. The layer was confirmed by EDS analysis to be a silica gel (with an average molar Si/O ratio of 1:4). On the contrary, the morphology of C_2MS_2 after corrosion was different from C_3MS_2: no new phase was formed on the corroded surface (Fig. 6b). Quantitative EDS spot analyses showed that the elemental composition was Si and O and traces of Ca and Mg.

Furthermore, a white flocculent precipitate was observed in the leachate of C_3MS_2 after two weeks of leaching; the same had been observed in the slag leachate under the ammonium chloride solution leaching [32]. The precipitate formed was identified to contain Si and O by EDS, which has the same phase composition as the layer obtained at the C_3MS_2 phase surface after corrosion. Therefore, the silica gel formed on the corrosion surface of C_3MS_2 is derived from the polymerization of silica [33, 34]. In contrast, no white precipitate was found in the C_2MS_2 leachate, indicating that most of the Si remains in the bulk phase without being dissolved and derives a Ca-depleted siliceous layer.

These different dissolution behaviors of Si in C_3MS_2 and C_2MS_2 are apparently related to the crystal structure of minerals, schematically shown in Fig. 7. The $[SiO_4]^{4-}$ tetrahedra and the strongly distorted cation-polyhedra are typical features of the silicates. The difference between C_2MS_2 and C_3MS_2 lies in the association of $[SiO_4]^{4-}$ tetrahedral units, as shown in Fig. 7b and Fig. 7d. Figure 8 presents schematically the leaching mechanism of C_3MS_2 and C_2MS_2 under the studied condition. Generally, minerals dissolution is the macroscopic manifestation of bond breakage in crystals. Acid-assisted dissolution preferentially breaks the M–O (M = Ca, Mg) bond due to the weak bond energy, leading to protonation, forming -Si–O–H groups [35, 36]. Therefore, both C_3MS_2 and C_2MS_2 can release Ca and Mg into the solution. Since the $[SiO_4]^{4-}$ tetrahedron is isolated in the C_3MS_2 crystal, H^+ can easily replace cations and form -Si–O–H groups in the solution (Fig. 8b). Two or more -Si–O–H groups aggregate and form a relatively dense silica gel precipitate [33, 37], as shown in Fig. 8a. Therefore, further decomposition of the C_3MS_2 phase is limited by the rate at which species move across the interface of the silica gel [38, 39].

However, two $[SiO_4]^{4-}$ tetrahedra sharing corners form a more complex dimer structure ($[Si_2O_7]^{6-}$) in C_2MS_2 (Fig. 7d). Figure 8d shows the C_2MS_2 reaction pathway of the dissolution occurring in the acidic solution in two steps. The dissolution of minerals would prefer to break the weaker bond. Thus, the protons give priority to breaking

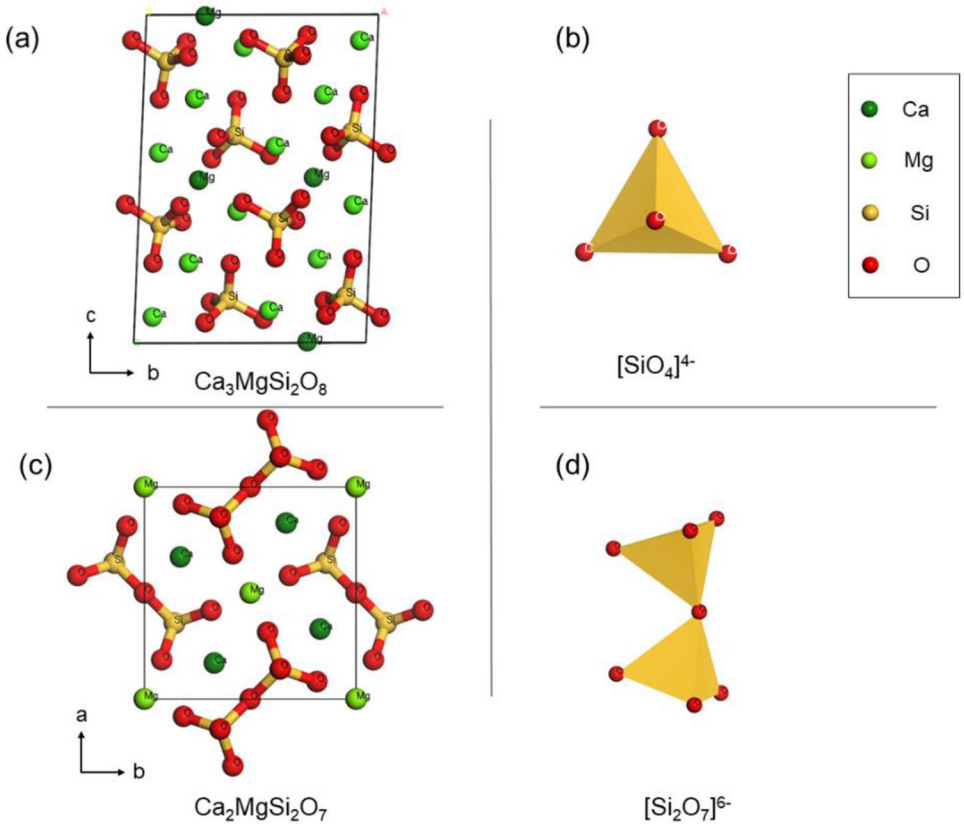

Fig. 7 **a** Crystal structure of C_3MS_2 with **b** an isolated silica tetrahedron $[SiO_4]^{4-}$ and **c** crystal structure of C_2MS_2 **d** with a dimer unit $[Si_2O_7]^6$

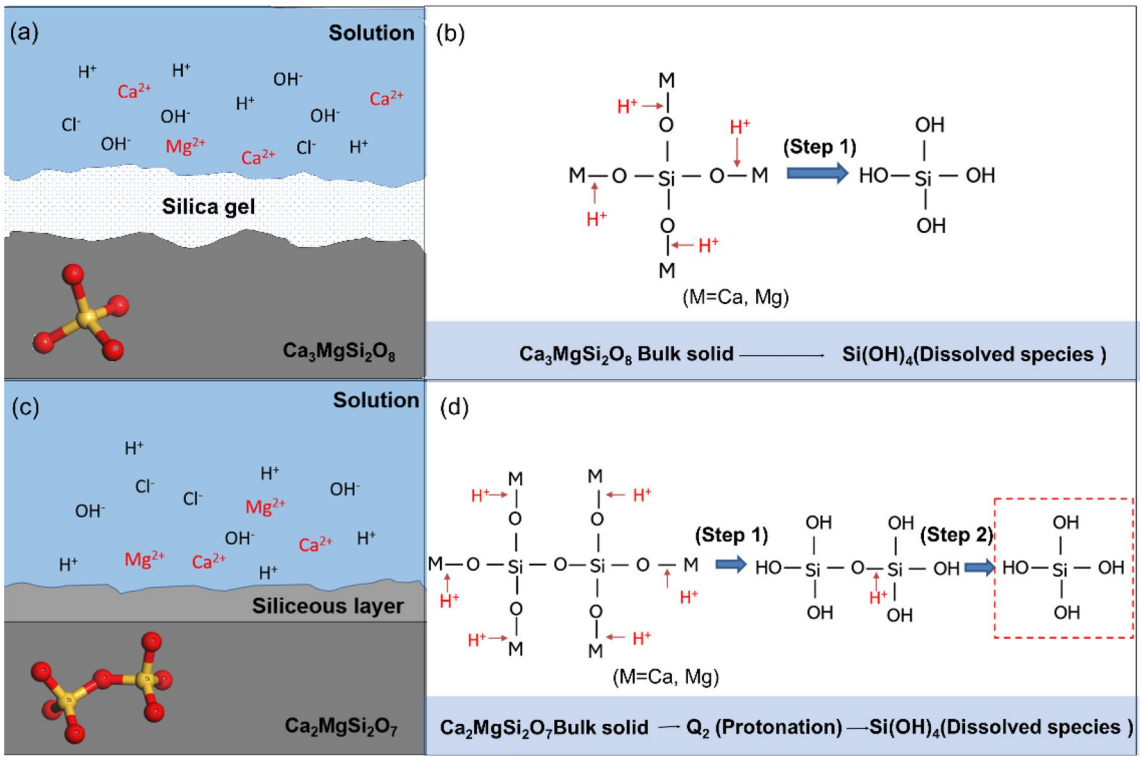

Fig. 8 Schematic diagram of the surface leaching behavior of **a** C_3MS_2 and **c** C_2MS_2 in 0.1 mol·L^{-1} HCl, and leaching mechanisms of **b** C_3MS_2 and **d** C_2MS_2

the O–M (M = Ca, Mg) bonds, leading to the formation of -Si–O–H groups (step 1). It is widely accepted that only the Si group present in the minerals as a small molecular weight unit or decomposed into small groups by a strong acid, Si group can be dissolved into the solution and with the further dissolution of cations [21]. Since the -Si–O-–Si groups exist in the dimer structure ($[Si_2O_7]^{6-}$), the macromolecular group cannot be directly dissolved, except for that the Si–O bonds are broken by protons (step 2) [40]. Based on the fact that no new phase was observed on the corroded surface of C_2MS_2, but instead a Ca-depleted siliceous layer, it can be concluded that the bridge oxygen bond in the C_2MS_2 crystal was obviously not broken by protons. Thus, only the first step of decomposition of C_2MS_2 occurs under the experimental acid conditions. Hence, a higher concentration of H^+ may be needed to completely decompose the C_2MS_2 phase due to the high strength of the Si–O bonds [41]. Therefore, the nature of crystal structure of the mineral plays a central role for the dissolution.

Aluminates

Figure 9 shows the morphological features of the three aluminate minerals before and after leaching in 0.1 mol·L^{-1} HCl solution for 48 h. It can be observed that the precipitates unevenly covered the $C_{12}A_7$ and C_3A surfaces after leaching and exhibited a non-uniform etch pit and corrosion depth (Fig. 9b, c). Furthermore, numerous flocculent precipitates separated from the C_3A and $C_{12}A_7$ leachates after two weeks also proved that the new phase formed after leaching. Work shown demonstrated that the solution first becomes supersaturated with respect to an aluminum hydroxide phase. In this work, the EDS results also confirmed that the new phase was aluminum hydroxide. The coupled interfacial dissolution-re-precipitation (CIDR) can describe the dissolution behavior of C_3A and $C_{12}A_7$ under the studied conditions [42, 43]. In addition, a Ca-depleted layer also derived on the $C_{12}A_7$ surface after corrosion, which contained Al, O, and trace of Ca by EDS. The results indicated that most of the Al remains in the bulk phase without being dissolved. For CA, small etch pits and cracks appeared on the surface during leaching (Fig. 9a). EDS results indicated that the corroded surface contained Ca, Al, and O and a significant decrease in Ca/Al ratio at the surface, which indicates that a Ca-depleted layer was left after Ca dissolution for 48 h. Therefore, C_3A shows higher leachability than $C_{12}A_7$ and CA, which is consistent with the results obtained from the leaching test in Sect. Leaching behavior. The formation and adsorption of a new amorphous phase on the surface of C_3A is the main obstacle for further leaching. In contrast, the inertness of CA is mainly due to the complex crystal structure. The leaching of $C_{12}A_7$ is dually affected by the adsorption of the new

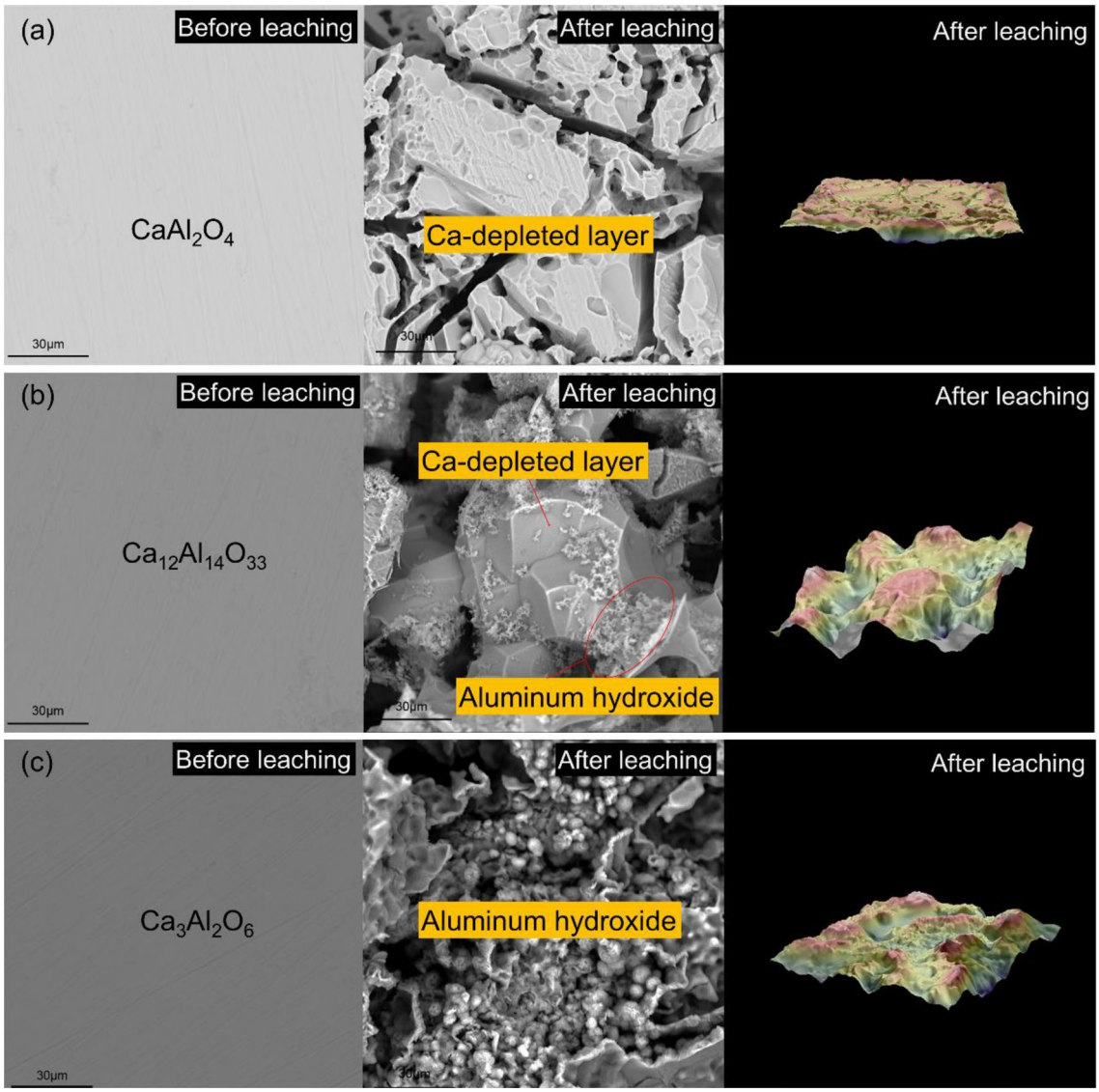

Fig. 9 SEM images and 3DMLM images of **a** CA, **b** $C_{12}A_7$, and **c** C_3A briquettes before and after leaching in 0.1 mol·L^{-1} HCl for 48 h and 90 °C drying for 10 h

phase of aluminum hydroxide and the crystal structure under the studied conditions.

Figure 10 shows the crystal structure of C_3A with cubic unit cell and reaction pathway of the C_3A dissolution occurring in the acidic solution. C_3A is composed of a closed six-member ring of aluminum tetrahedra ($[Al_6O_{18}]^{18-}$) and calcium polyhedral stacking [44]. The dissolution process of the C_3A phase in the acidic solution is divided into three steps. Due to the relatively stable closed ring structure, the H^+ ion in the solution first attacks the CaO bond and forma an $[Al_6O_{18}H_{12}]^{6-}$ group (cf. Figure 10c) [45]. The remaining H^+ will destroy the six-membered aluminum ring and decompose it into small molecular weight groups in the solution ($Al(OH)_4^+$) as depicted in Fig. 10d [46]. Finally, the dissolved $Al(OH)_4^+$ ions precipitate and are adsorbed on the C_3A surface. In the C_3A, $C_{12}A_7$, and CA phases, the molar ratio of Ca/Al in the aluminates decreases from 1.5 to 0.5, which makes the association of six-membered ring ($[Al_6O_{18}]^{18-}$) in the crystal become more complicated. The work of Fabian and co-workers [25] suggested that the non-bridging oxygen (NBO) over the Al-tetrahedral structure (T) index shows that the atomic structure may affect the leaching extent of the synthetic calcium aluminate slags. The manner of association of Al-tetrahedron in the crystal characterizes the complexity of crystal structure, which has the same effect as the NBO/T index and can evaluate the sensitivity of phase leaching to a certain extent. $C_{12}A_7$ is here composed of a positively charged framework, $[Ca_{24}Al_{28}O_{64}]^{4+}$, with 12 subnanometer-sized cages in a cubic unit cell [47]. In the CA crystal structure, $[AlO_4]^{5-}$ tetrahedra are bonded to

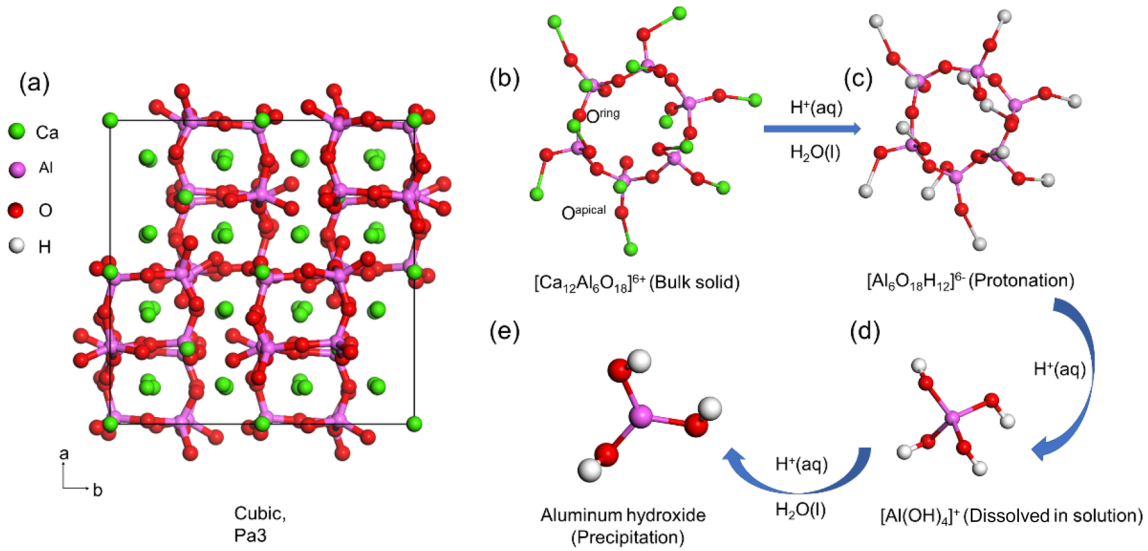

Fig.10 **a** Crystal structure of C_3A with cubic unit cell, and C_3A reaction pathway of the dissolution occurring in the acidic solution from **b** to **e**

each other and form a network structure. The complexity of crystal structure increases from the ring framework to the network, which indicates that a higher H^+ concentration is needed to attack the Al-O network structure and decompose the aluminates fully. Therefore, under the acid concentration in this experiment (0.1 mol·L^{-1} HCl), H^+ can severely disintegrate the structure of ring in C_3A, and partially destroy the framework structure in the $C_{12}A_7$, while having a very weak effect on the network structure in the CA.

Ferrite

Figure 11 shows 3DMLM and SEM images of the C_2F briquette before and after leaching. The C_2F gave similar result as CA and C_2MS_2 when it comes to changes of morphology transformation before and after corrosion. EDS results indicate that the chemical composition of the corroded surface contains Fe and O and traces of Ca. SEM–EDS analysis revealed that the Ca-depleted layer was obtained after C_2F extraction in the acidic solution. Some Fe also dissolved from the bulk phase and the leachate was light yellow (Fe^{3+}). A more considerable amount of Fe remains in the bulk phase due to the chain structure of Fe polyhedron. Figure 12 shows the crystal structure of C_2F. In the experiments of this work, the acidity of the solution was not strong enough to attack the oxo-bridged oxygen bond in the single-chain polyhedron. Based on the results of the poor leaching yield of powder C_2F (Fig. 5) and morphological feature of the Ca-depleted layer left on the corroded surface, it is reasonable to believe that no decomposition or partial decomposition of the chain structure occurs upon acid track.

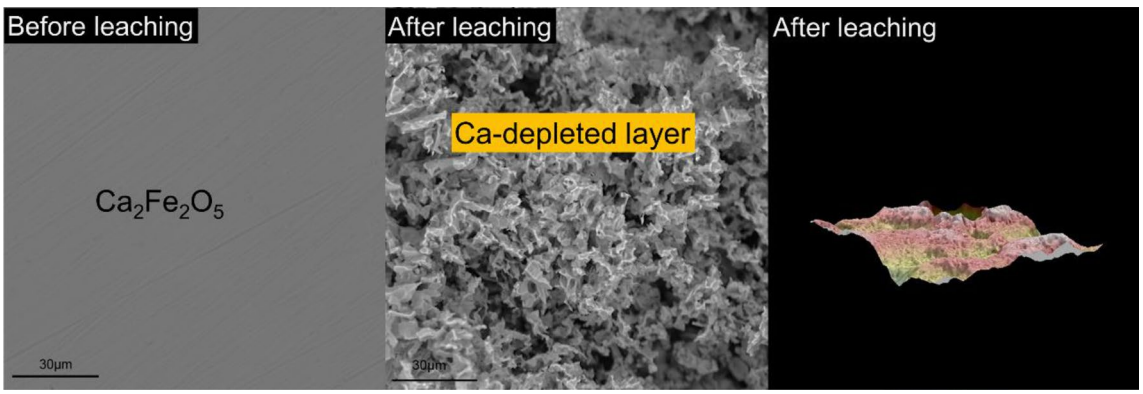

Fig. 11 SEM images and 3DMLM image of C_2F briquette before and after 0.1 mol·L^{-1} HCl leaching for 48 h and 90 °C

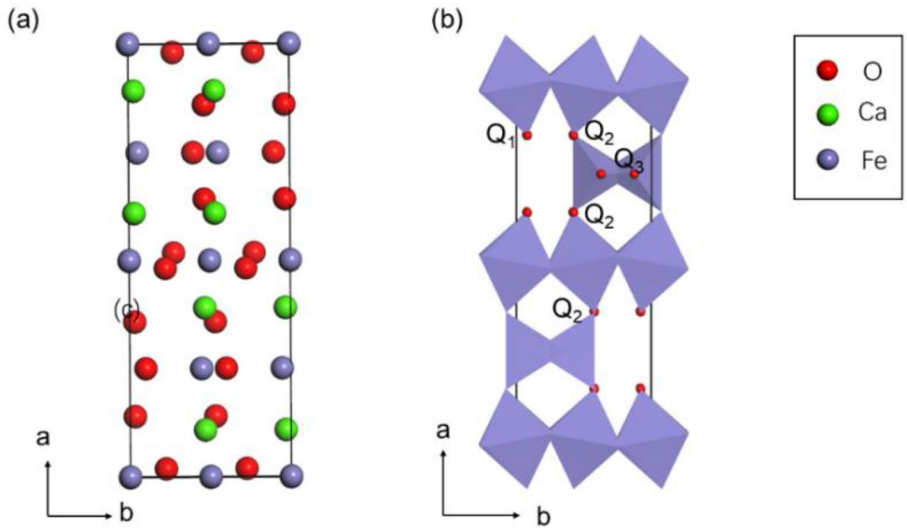

Fig. 12 **a** Lattice diagram and **b** iron polyhedron diagram of C_2F crystal structure

Conclusions

The leachability of common minerals in steel slag ((Ca/Mg)-silicates, -aluminates, -ferrites, and oxides) in an acidic solution was evaluated by thermodynamic analysis. Furthermore, seven principal Ca- and Mg-bearing phases (γ-C_2S, C_2MS_2, C_3MS_2, CA, $C_{12}A_7$, C_3A, and C_2F) were synthesized and a series of leaching tests were carried out to study the feasibility for later application in CO_2 capture. CaO showed a high Ca leachability in an acidic solution, followed by C_3A and silicate phases, while $C_{12}A_7$, CA, and C_2F phases showed a relatively poor Ca dissolution characteristics. The incomplete dissolution of Ca-bearing phases was attributed to the crystal structure feature and the formation of precipitated phases. Under the experimental conditions applied, the dissolution of C_3MS_2, $C_{12}A_7$, and C_3A phases was accompanied by the release of elements and the formation of new phases. A precipitated silica gel and aluminum hydroxide may cover the surface of the particles hindering a further decomposition. In the dissolution processes of C_2MS_2, $C_{12}A_7$, C_2F, and CA phases, more Ca was leached than Si, Fe, and Al elements, resulting in a Ca-depleted layer at the surface of the particles. Thus, the difference in dissolution behavior of the elements is indeed related to the crystal structure of the minerals.

The study confirms that phase modification of SS before SS-CCUS is necessary because some Ca is enriched in the refractory minerals, such as CA and C_2F phases. In addition, the results discussed in this paper also give valuable information on phase modification of SS for CO_2 sequestration, which makes Ca and Mg enriched in CaO, C_3A, and silicates for improving Ca extraction yield. Moreover, the future work will study of phase modification of SS through controlling the crystallization process of the molten slag. The modified SS will be used for indirect carbon capture to reduce CO_2 emissions and simultaneously the amount of SS.

Acknowledgements The authors gratefully acknowledge support by the National Natural Science Foundation of China (No. 52074078), the Liaoning Provincial Natural Science Foundation of China (No. 2019–MS–127), the National Training Program of Innovation and Entrepreneurship for Undergraduates (No. 210089), and the Fundamental Research Funds for the Central Universities (No. N2124001, N2025035, and N2125034).

Declarations

Conflict of interest The authors declare that they have no conflict of interest.

References

1. Guo J, Bao Y, Wang M (2018) Steel slag in China: treatment, recycling, and management. Waste Manag 78:318–330. https://doi.org/10.1016/j.wasman.2018.04.045
2. Ostovari H, Sternberg A, Bardow A (2020) Rock "n" use of CO_2: carbon footprint of carbon capture and utilization by mineralization. SUT J Math. https://doi.org/10.1039/d0se00190b
3. Ibrahim M, El-Naas M, Benamor A, Al-Sobhi S, Zhang Z (2019) Carbon mineralization by reaction with steel-making waste: a review. Processes 7:115. https://doi.org/10.3390/pr7020115
4. Selamat SN, Nor NHM, Rashid MHA, Ahmad MF, Mohamad F, Ismail AE, Hassan MF, Turan FM, Zain MZM, Bakar EA, Seiji Y (2017) Review of CO_2 reduction technologies using mineral carbonation of iron and steel making slag in Malaysia. J Phys Conf Ser 914:012012. https://doi.org/10.1088/1742-6596/914/1/012012
5. Teir S (2008) Fixation of carbon dioxide by producing carbonates from minerals and steelmaking slags. (Doctoral dissertation). Helsinki University of Technology, Finland
6. Eloneva S (2010) Reduction of CO2 emissions by mineral carbonation: steelmaking slags as raw material with a pure calcium carbonate end product. (Doctoral dissertation). Aalto University, Finland

7. Hall C, Large DJ, Adderley B (2014) Calcium leaching from waste steelmaking slag: significance of leachate chemistry and effects on slag grain mineralogy. Miner Eng 65:156–162. https://doi.org/10.1016/j.mineng.2014.06.002
8. Zhao Q, Chu XY, Mei XH, Meng QZ, Li JY, Liu CJ, Henrik S, Ron Z (2020) Co-treatment of waste from steelmaking processes: steel slag-based carbon capture and storage by mineralization. Front Chem 8:1–7. https://doi.org/10.3389/fchem.2020.571504
9. Doucet FJ (2010) Effective CO_2-specific sequestration capacity of steel slags and variability in their leaching behavior in view of industrial mineral carbonation. Miner Eng 23:262–269. https://doi.org/10.1016/j.mineng.2009.09.006
10. Ragipani R, Bhattacharya S, Akkihebbal SK (2020) Understanding dissolution characteristics of steel slag for resource recovery. Waste Manage 117:179–187. https://doi.org/10.1016/j.wasman.2020.08.008
11. Wan XW, Chen M, Qiu YC, Qiu YC, Shi JJ, Li JZ, Liu CS, Pekka T, Ari J (2020) Influence of manganese oxide on the liquid-perovskite equilibrium in the CaO-SiO_2 -TiO_2 system at 1400 °C in air [J]. Ceram Int. https://doi.org/10.1016/j.ceramint.2020.12.241
12. Zhao Q, Liu K, Sun LF, Liu CJ, Henrik JMF, S, and Ron Z, (2020) Towards carbon sequestration using stainless steel slag via phase modification and co-extraction of calcium and magnesium. Process Saf Environ Prot 133:73–81. https://doi.org/10.1016/j.psep.2019.11.004
13. Li J, Mou QQ, Zeng Q, Yu Y (2019) Experimental study on precipitation behavior of spinels in stainless steel-making slag under heating treatment. Processes 7(8):487. https://doi.org/10.3390/pr7080487
14. Liu CJ, Qiu JY, Liu ZY, Zhu DY, Wang YG (2020) Phase equilibria in the system CaO-SiO2-Nb2O5-La2O3 at 1473 K with PO2=10–15.47 atm. Ceram Int 46(4):7711–7718. https://doi.org/10.1016/j.ceramint.2019.11.274
15. Liu CJ, Qiu JY (2018) Phase equilibrium relations in the specific region of CaO-SiO_2-La_2O_3 system. J Eur Ceram Soc 38(4):2090–2097. https://doi.org/10.1016/j.jeurceramsoc.2017.12.011
16. Nath M, Song S, Garbers-Craig AM, Li YW (2018) Phase evolution with temperature in chromium-containing refractory castables used for waste melting furnaces and Cr(VI) leachability. Ceram Int 44(16):20391–20398. https://doi.org/10.1016/j.ceramint.2018.08.032
17. Song S, Garbers-Craig AM (2016) Formation, leachability and encapsulation of hexavalent chromium in the Al_2O_3 –CaO–Fe_2O_3 –Cr_2O_3 system. J Eur Ceram Soc 36(6):1479–1485. https://doi.org/10.1016/j.jeurceramsoc.2015.12.036
18. Zhao Q, Liu C, Gao T, Gao L, Saxén H, Zevenhoven R (2019) Remediation of stainless steel slag with MnO for CO_2 mineralization. Process Saf Environ Prot. https://doi.org/10.1016/j.psep.2019.04.025
19. Zhang HN (2013) Alkaline extraction characteristics of steelmaking slag batch in NH_4Cl solution under environmental pressure. J Cent South Univ 20:1482–1489. https://doi.org/10.1007/s11771-013-1638-0
20. Said A, Mattila O, Eloneva S, Järvinen M (2015) Enhancement of calcium dissolution from steel slag by ultrasound. Chem Eng Process 89:1–8. https://doi.org/10.1016/j.cep.2014.12.008
21. Terry B (1983) The acid decomposition of silicate minerals part I. Reactivities and modes of dissolution of silicates. Hydrometallurgy 10:135–150. https://doi.org/10.1016/0304-386X(83)90002-6
22. Zhao Q, Li JY, You KW, Liu CJ (2019) Recovery of calcium and magnesium bearing phases from Iron– and steelmaking slag for CO_2 sequestration. Process Saf Environ Prot 135:81–90. https://doi.org/10.1016/j.psep.2019.12.012
23. Haynes WM (2016) Crc handbook of chemistry and physics, 96th edn. CRC Press, Boca Raton
24. Wen RS (1990) Industrial petrology. China University of Geosciences Press, China
25. Azof FI, Yang Y, Panias D, Kolbeinsen L, Safarian J (2019) Leaching characteristics and mechanism of the synthetic calcium-aluminate slags for alumina recovery. Hydrometallurgy. https://doi.org/10.1016/j.hydromet.2019.03.006
26. Jost KH, Ziemer B, Seydel R (1977) Redetermination of the structure of β-dicalcium silicate. Acta Crystallogr A 33:1696–1700. https://doi.org/10.1107/S0567740877006918
27. Toraya H (1986) Whole-powder-pattern fitting without reference to a structural model: application to X-ray powder diffraction data. J Appl Crystallogr 19:440–447. https://doi.org/10.1107/S0021889886088982
28. Bonenfant D, Kharoune L, Sauvé S, Hausler R, Niquette P, Mimeault M, Kharoune M (2008) CO_2 sequestration potential of steel slags at ambient pressure and temperature. Ind Eng Chem Res 47:7610–7616. https://doi.org/10.1021/ie701721j
29. Pérez-López R, Montes-Hernandez G, Nieto JM, Nieto JM, Renard F, Charlet L (2008) Carbonation of alkaline paper mill waste to reduce CO_2 greenhouse gas emissions into the atmosphere. Appl Geochem 23:2292–2300. https://doi.org/10.1016/j.apgeochem.2008.04.016
30. Lekakh SN, Rawlins CH, Robertson DGC, Richards VL, Peaslee KD (2008) Kinetics of aqueous leaching and carbonization of steelmaking slag. Metall Mater Trans B 39B:125–134. https://doi.org/10.1007/s11663-007-9112-8
31. Hou J, Chen Z, Liu J (2020) Hydration activity and expansibility model for the RO phase in steel slag. Metall Mater Trans B 51:1–8. https://doi.org/10.1007/s11663-020-01847-3
32. Hall C, Large DJ, Adderley B, West HM (2104) Calcium leaching from waste steelmaking slag: significance of leachate chemistry and effects on slag grain mineralogy [J]. Mineral Eng 65:156–162
33. Terry B (1983) The acid decomposition of silicate minerals part II. Hydrometallurgical Application Hydrometallurgy 10(2):151–171. https://doi.org/10.1016/0304-386x(83)90003-8
34. Brantley SL (2003) Reaction kinetics of primary rock-forming minerals under ambient conditions. Treatise Geochem. https://doi.org/10.1016/b0-08-043751-6/05075-1
35. Baucke FGK (1994) Corrosion of glasses and its significance for glass coating. Electrochim Acta 39:1223–1228. https://doi.org/10.1016/0013-4686(94)E0040-7
36. Casey WH, Westrich HR, Arnold GW (1988) Surface chemistry of labradorite feldspar reacted with aqueous solutions at pH = 2, 3, and 12. Geochim Cosmochim Acta 52:2795–2807. https://doi.org/10.1016/0016-7037(88)90147-0
37. Crundwell FK (2014) The mechanism of dissolution of minerals in acidic and alkaline solutions: part II application of a new theory to silicates, aluminosilicates and quartz. Hydrometallurgy 149:265–275. https://doi.org/10.1016/j.hydromet.2014.07.003
38. Tsomaia N, Brantley SL, Hamilton JP, Pantano CG, Mueller KT (2003) NMR evidence for formation of octahedral and tetrahedral Al and repolymerization of the SI network during dissolution of aluminosilicate glass and crystal. Am Mineral 88:54–67. https://doi.org/10.2138/am-2003-0107
39. Daval D, Sissmann O, Menguy N, Saldi GD, Guyot F, Martinez I, Corvisier O, Garcia B, Machouk I, Knauss KG, Hellmann R (2011) Influence of amorphous silica layer formation on the dissolution rate of olivine at 90°C and elevated PCO_2. Chem Geol 284(1–2):193–209. https://doi.org/10.1016/j.chemgeo.2011.02.021
40. Brantley SL (2008) Kinetics of mineral dissolution. In: rantley, Susan, Kubicki, James,White, Art (Eds.), Kinetics of Water–Rock Interaction. Springer, New York.
41. Sun KH, Huggins ML (1947) Energy additivity in oxygen-containing crystals and glasses. J Phys Colloid Chem 51:438–443. https://doi.org/10.1021/j150448a003

42. Hellmann R, Wirth R, Daval D, Barnes JP, Penisson JM, Tisserand D, Hervig RL (2012) Unifying natural and laboratory chemical weathering with interfacial dissolution-reprecipitation: a study based on the nanometer-scale chemistry of fluid-silicate interfaces. Chem Geol 294–295:203–216. https://doi.org/10.1016/j.chemgeo.2011.12.002
43. Hellmann R, Cotte S, Cadel E, Malladi S, Karlsson LS, Lozano-Perez S, Cabiè M, Seyeux A (2015) Nanometre-scale evidence for interfacial dissolution–reprecipitation control of silicate glass corrosion. Nat Mater 14(3):307–311. https://doi.org/10.1038/nmat4172
44. Mondal P, Jeffery JW (1975) The crystal structure of tricalcium aluminate, $Ca_3Al_2O_6$. Acta Crystallogr Sect B: Struct Crystallogr Cryst Chem 31:689–697. https://doi.org/10.1107/s0567740875003639
45. Bauer A, Velde BD (2014) Geochemistry at the earth's surface https://doi.org/10.1007/978-3-642-31359-2
46. Brand AS, Bullard JW (2017) Dissolution kinetics of cubic tricalcium aluminate measured by digital holographic microscopy. Langmuir 33:9645–9656. https://doi.org/10.1021/acs.langmuir.7b02400
47. Kim KB, Kikuchi M, Miyakawa YH, Kamiya T, Hirano M, Hosono H (2007) Photoelectron spectroscopic study of $C_{12}A_7$: e-and Alq3 Interface: the formation of a low electron-injection barrier. J Phys Chem C 111:8403–8406. https://doi.org/10.1021/jp072635r